Uranium isotope evidence for two episodes of deoxygenation during Oceanic Anoxic Event 2

Matthew O. Clarkson[a,1,2], Claudine H. Stirling[a], Hugh C. Jenkyns[b], Alexander J. Dickson[b,c], Don Porcelli[b], Christopher M. Moy[d], Philip A. E. Pogge von Strandmann[e], Ilsa R. Cooke[a], and Timothy M. Lenton[f]

[a]Department of Chemistry, University of Otago, Dunedin 9054, New Zealand; [b]Department of Earth Sciences, University of Oxford, Oxford OX1 3AN, United Kingdom; [c]Department of Earth Sciences, Royal Holloway University of London, Egham TW20 0EX, United Kingdom; [d]Department of Geology, University of Otago, Dunedin 9054, New Zealand; [e]London Geochemistry and Isotope Centre, Institute of Earth and Planetary Sciences, University College London and Birkbeck, University of London, London WC1E 6BT, United Kingdom; and [f]Earth System Science, College of Life and Environmental Sciences, University of Exeter, Exeter EX4 4QE, United Kingdom

Edited by Thure E. Cerling, University of Utah, Salt Lake City, UT, and approved January 22, 2018 (received for review August 30, 2017)

Oceanic Anoxic Event 2 (OAE 2), occurring ∼94 million years ago, was one of the most extreme carbon cycle and climatic perturbations of the Phanerozoic Eon. It was typified by a rapid rise in atmospheric CO_2, global warming, and marine anoxia, leading to the widespread devastation of marine ecosystems. However, the precise timing and extent to which oceanic anoxic conditions expanded during OAE 2 remains unresolved. We present a record of global ocean redox changes during OAE 2 using a combined geochemical and carbon cycle modeling approach. We utilize a continuous, high-resolution record of uranium isotopes in pelagic and platform carbonate sediments to quantify the global extent of seafloor anoxia during OAE 2. This dataset is then compared with a dynamic model of the coupled global carbon, phosphorus, and uranium cycles to test hypotheses for OAE 2 initiation. This unique approach highlights an intra-OAE complexity that has previously been underconstrained, characterized by two expansions of anoxia separated by an episode of globally significant reoxygenation coincident with the "Plenus Cold Event." Each anoxic expansion event was likely driven by rapid atmospheric CO_2 injections from multiphase Large Igneous Province activity.

oceanic anoxia | OAE | uranium isotopes | biogeochemical model | carbon cycle

Rapid climatic warming events have repeatedly punctuated Earth's history and have often been associated with prolonged episodes of widespread oceanic anoxia. These intervals represent major disturbances to the global carbon cycle, which contributed to marine faunal turnover and mass extinctions (1). In particular, the Mesozoic Era was characterized by numerous prolonged intervals of globally enhanced anoxia, termed "Oceanic Anoxic Events" (OAEs) (1). The Mesozoic OAEs are considered the model expression of oceanic anoxia in the Phanerozoic geological record, thus informing studies of past hyperthermal events and future environmental change (2, 3). Despite extensive study, the magnitude and timing of oceanic anoxia for OAEs are still poorly constrained, representing a fundamental limitation for defining these events. We address this shortcoming by presenting a quantitative record of oceanic anoxia for OAE 2.

OAE 2 is the most widely recognized and severe OAE, occurring at the Cenomanian–Turonian Boundary (∼94 Ma) (1) and lasting for up to ∼900 thousand years (ky) (4). A leading hypothesis for the initiation of OAE 2 is through the emplacement of one or more of the Caribbean, Madagascar, and High-Arctic Large Igneous Provinces (LIPs) (1, 5–7) and an associated outgassing of CO_2 that caused climate warming and accelerated weathering (8). Such processes likely drove an increase in the supply of nutrients, especially phosphorus (P), to the ocean, and thereby increased productivity and oxygen demand through the aerobic degradation of organic matter (1, 5, 9). Productivity was potentially further amplified by the effective recycling of P from sediments overlain by anoxic waters (10–12). Ultimately, this chain of events led to anoxic water column conditions and the enhanced preservation of organic carbon, which formed distinct black shales in marine sedimentary successions in many ocean basins. The preferential burial of isotopically light carbon (C) also contributed to a broad positive carbon isotope excursion (CIE) across OAE 2 that is utilized as a global chemostratigraphic marker of the event (1). Silicate weathering and organic carbon burial are vital components of the global carbon cycle and represent important negative feedback mechanisms that sequester atmospheric CO_2 and drive climate stabilization during global warming events (8, 12, 13). However, the detailed behavior of these recovery processes is currently limited for numerous carbon cycle perturbations in Earth history, including OAEs.

For OAE 2, there is widespread evidence of regionally extensive anoxia and euxinia (anoxic sulfidic water column conditions) in disparate localities, leading to benthic faunal extinctions, globally enhanced organic carbon burial, and the sequestration of redox-sensitive and chalcophilic trace metals (1, 9, 12, 14, 15). Oceanic anoxia is, however, a spatially heterogeneous condition, with a highly variable geochemical and sedimentary expression. A dependence on local redox indicators has significantly limited the integration of this important phenomenon into a global carbon cycle framework. To address this limitation, we present a quantitative record of the global extent of anoxia for OAE 2 using, high-resolution uranium (U) isotope ($^{238}U/^{235}U$, reformulated as $\delta^{238}U$; see *Supporting Information*) data, in combination with a biogeochemical model that calculates changes in the coupled global C, P, and U cycles.

Significance

Past "Oceanic Anoxic Events" (OAEs) represent important carbon cycle perturbations that offer the opportunity to study Earth's response to extreme climate warming. A fundamental limitation for understanding OAEs is quantifying the timing and total extent of ocean anoxia. We present a quantitative account of global redox conditions for OAE 2 (∼94 million years ago), using a high-resolution record of uranium isotopes combined with a biogeochemical model. We present new evidence for two discrete intervals of globally extensive anoxia that were coupled to enhanced terrestrial weathering, within the typically defined OAE interval. These anoxic intervals were separated by ocean reoxygenation and the temporary recovery of the carbon cycle.

Author contributions: M.O.C., C.H.S., H.C.J., D.P., C.M.M., and T.M.L. designed research; M.O.C., C.H.S., A.J.D., P.A.E.P.v.S., I.R.C., and T.M.L. performed research; A.J.D. contributed new reagents/analytic tools; M.O.C., C.H.S., H.C.J., P.A.E.P.v.S., and T.M.L. analyzed data; M.O.C., C.H.S., and T.M.L. wrote the paper; and H.C.J. provided samples.

The authors declare no conflict of interest.

This article is a PNAS Direct Submission.

[1]Present address: Institute of Geochemistry and Petrology, Department of Earth Sciences, Eidgenössische Technische Hochschule Zürich (ETHZ), 8092 Zürich, Switzerland.

[2]To whom correspondence should be addressed. Email: matthew.clarkson@erdw.ethz.ch.

This article contains supporting information online at www.pnas.org/lookup/suppl/doi:10.1073/pnas.1715278115/-/DCSupplemental.

Published online March 5, 2018.

These geochemical data come from well-preserved and extensively studied carbonate sediments that were deposited under oxygenated conditions in the European shelf sea and Tethyan continental margin during OAE 2. The studied sections (Fig. 1) include deeper shelf pelagic foraminiferal–nannofossil carbonates (chalks) from Eastbourne and South Ferriby (United Kingdom), and shallow-water platform carbonates from Raia del Pedale (Italy). We also present additional lithium isotope data [$^{7}Li/^{6}Li$, reformulated as $\delta^{7}Li$ (8)] for Eastbourne, which supplement previously published results (8) to give a more highly resolved complementary record of changes in the global weathering regime during OAE 2.

Under anoxic conditions, oxidized and soluble U(VI) is drawn down from the water column and deposited in sediments as reduced and immobile U(IV), driving seawater U concentrations ([U]) to lower values (16, 17). The primary isotopic fractionation of U is also strongly redox-dependent, whereby ^{238}U is preferentially sequestered in anoxic sediments, leaving the residual seawater relatively enriched in ^{235}U (18–25). This geochemical behavior generates lower $\delta^{238}U$ signatures in seawater that can be recorded in contemporary sediments. Moreover, because of the long residence time of U in the modern ocean [320 ky to 560 ky (16)], sedimentary $\delta^{238}U$ signatures can resolve global changes in oceanic redox conditions (14, 26–29), which cannot be achieved by more traditional proxies.

For OAE 2, application of the U isotope paleoredox tracer is limited to a single study of organic-rich black shales ($\delta^{238}U_{shale}$), wherein the data are suggestive of a threefold increase in the extent of anoxia across the event (14). These data (Fig. 1) are of insufficient temporal resolution to provide insights into the rate and magnitude of ocean redox changes across the event or elucidate the temporal relationship of ocean anoxia to other aspects of the Earth system response. Furthermore, the fractionation of U into black shales is strongly influenced by local geochemical controls (30) that complicate attempts to infer the "global" U isotope signature of oceanic redox changes. By contrast, the U isotope signature of primary carbonate precipitates ($\delta^{238}U_{carb}$) records the seawater isotopic composition ($\delta^{238}U_{sw}$), with minimal additional fractionation under most environmental conditions (21, 25, 31, 32).

The datasets presented here are used to test the current hypotheses for OAE 2 initiation, and the resulting biogeochemical changes, by acting as target outputs for the C–P–U model (see *Materials and Methods* and *Supporting Information*). This approach differs from other efforts to model U isotope data in deep time (14, 26–29), in that it calculates dynamic changes to the wider Earth system, including temperature, weathering, nutrient inputs, anoxia, and carbon burial, driven by hypothesized perturbations to the carbon cycle. These changes, in turn, affect the oceanic U cycle. The benefit of this approach is that it gives an internally consistent, quantitative assessment of coupled changes in the carbon cycle.

Results and Discussion

Geochemical Reconstruction of Oceanic Anoxia. The stratigraphically expanded Eastbourne section has been extensively studied for a multitude of paleoenvironmental proxies, owing to its lack of significant diagenetic alteration (1, 8, 15, 33, 34) (*Supporting Information*). In particular, the carbonates from Eastbourne have very low values of total organic carbon (TOC) (34) and were not subject to appreciable diagenetic sulfate reduction in pore waters (33), which should have minimized alteration of the primary $\delta^{238}U_{carb}$ signatures. As such, the $\delta^{238}U_{carb}$ record for Eastbourne should closely reflect variability in $\delta^{238}U_{sw}$ throughout the OAE 2 interval and is hence used as the primary reference curve in the present study. The $\delta^{238}U_{carb}$ record for Eastbourne has the highest resolution of the three sites, and systematic temporal trends are statistically identified using a locally weighted polynomial smoothing function (LOESS) to prevent undue emphasis being placed on single data points. The South Ferriby section, although also showing a low degree of diagenetic alteration (*Supporting Information*), is more lithified than Eastbourne, raising the possibility of greater secondary influences on $\delta^{238}U_{carb}$. It also contains a significant unconformity (Fig. 1), which is overlain by an organic-rich black shale. Mobilization of U from this horizon could potentially explain the comparatively high $\delta^{238}U_{carb}$ values above the unconformity that are more typical of anoxic sediments (18, 19, 23, 30). Deposits at Raia del Pedale show evidence for partial recrystallization and dolomitization of originally mixed aragonite and high-magnesium-calcite producers (*Supporting Information*). In particular, the lowest $\delta^{238}U_{carb}$ of the section are from dolomitized samples with anomalously high U/Ca (Fig. 1 and Fig. S3), consistent with the negative $\delta^{238}U_{carb}$ offset and U enrichment observed in modern dolomites (21, 31).

Multiple lines of evidence support the fidelity of the Eastbourne $\delta^{238}U_{carb}$ record. First, despite potential diagenetic influences in the Raia del Pedale and South Ferriby sections, stability is seen in the $\delta^{238}U_{carb}$ records postdating OAE 2 at all three sites (Fig. 1). It is important to note that, during this stable post-OAE 2 interval, $\delta^{238}U_{shale}$ values from the organic-rich black shales of Ocean

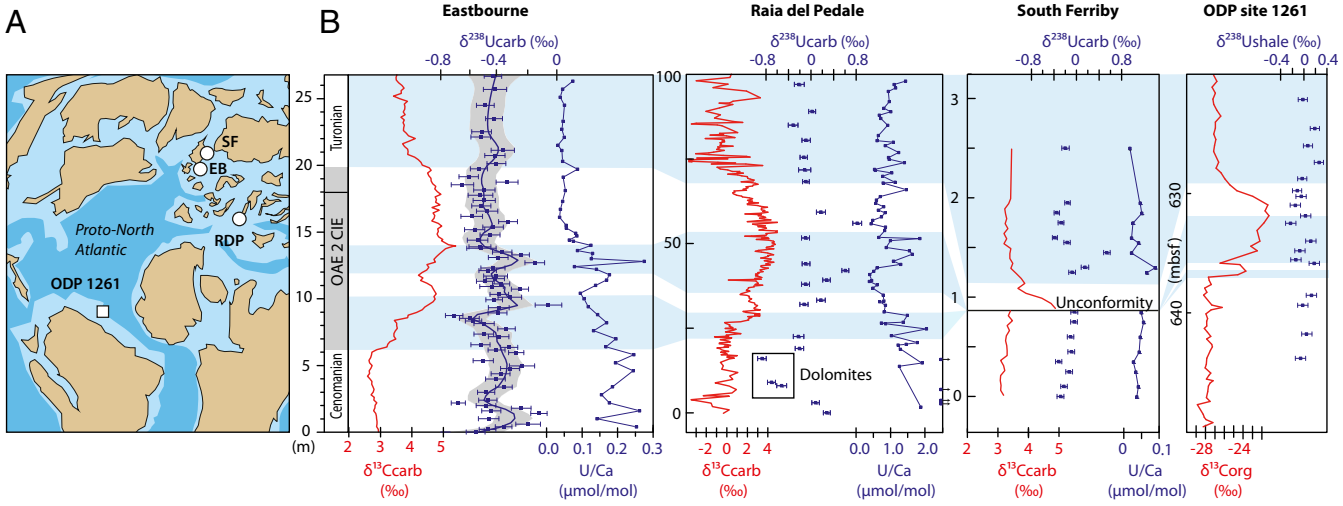

Fig. 1. (*A*) Paleogeographic reconstruction showing locations of Eastbourne (EB), Raia del Pedale (RDP), South Ferriby (SF), and ODP site 1261, modified with permission from ref. 67. (*B*) The $\delta^{13}C$ (15, 34, 68), $\delta^{238}U_{carb}$ (±2 SE), and U/Ca (ref. 35 and this study) for EB, RDP, and SF in comparison with $\delta^{13}C_{org}$ and $\delta^{238}U$ from black shales at ODP site 1261 (14, 55). Correlations (blue shading) are from previous work (8, 15, 35).

Drilling Program (ODP) site 1261 (14) are ~0.5‰ higher than contemporaneous $\delta^{238}U_{carb}$ (Fig. 1). This offset is consistent with the observed magnitude and direction of U isotope fractionation during U reduction in modern organic-rich sediments under an anoxic water column (18, 19, 23, 30) and therefore suggests that Eastbourne $\delta^{238}U_{carb}$ closely reflects absolute values in $\delta^{238}U_{sw}$. Furthermore, during this stable period, $\delta^{238}U_{carb}$ from Raia del Pedale and South Ferriby are ~0.2 to 0.3‰ higher than that from Eastbourne, which is consistent with observations from some modern bulk carbonate sediments that show higher $\delta^{238}U_{carb}$ than seawater due to early diagenesis (31). These offsets, compared with Eastbourne, therefore likely reflect the diagenetic gradient between the carbonate sites and support a near-primary $\delta^{238}U_{sw}$ signature at Eastbourne. In addition, there are two systematic decreases in $\delta^{238}U_{carb}$ at Eastbourne [Anoxia Expansion (AE) 1 and AE2, Fig. 2] which are associated with the progressive lowering of U/Ca and other redox-sensitive or chalcophilic trace metals (TM_{redox}) at multiple localities, consistent with the removal of these elements into anoxic sediments. Finally, there is a broad coupling between two decreases in the $\delta^{238}U_{carb}$ and $\delta^{7}Li$ records (Fig. 2), which would not be preserved during diagenesis, and substantiates the veracity of both datasets.

At Eastbourne, the onset of the CIE, which typically defines the beginning of OAE 2, is closely associated with a systematic decrease in $\delta^{238}U_{carb}$ from a maximum of −0.24 ± 0.09‰ (2 SE) to a minimum of −0.71 ± 0.06‰ (AE1). This drop in values is accompanied by a decrease in TM_{redox} in multiple localities (35–37), including Eastbourne (Figs. 1 and 2) and Raia del Pedale (Fig. 1), suggesting the global expansion of oceanic anoxic conditions. After AE1, $\delta^{238}U_{carb}$ rapidly increases to −0.41 ± 0.07‰, suggesting a decrease in the extent of oceanic anoxia. This dramatic change directly corresponds to the onset of the Plenus Cold Event (PCE), an interval characterized by cooler temperatures at a range of latitudes (35, 38–45). Higher $\delta^{238}U_{carb}$ values averaging −0.38 ± 0.12‰ (1 SD) were maintained throughout the PCE and correspond to widely observed TM_{redox} enrichments (35–37) (Figs. 1 and 2), indicating the decreased sequestration and oxidative liberation of these metals under more oxygenated conditions (35). The rise in $\delta^{238}U_{carb}$ is also consistent with observations of local benthic faunal repopulation and local reoxygenation in some basins, during the PCE (35, 36, 44–47). Importantly, the $\delta^{238}U_{carb}$ dataset indicates that the PCE reoxygenation was globally significant, returning the ocean to a redox state similar to preperturbation conditions.

The end of the PCE corresponds to a second systematic decrease in $\delta^{238}U_{carb}$ (AE2). Again, the concentrations of TM_{redox} decrease at both Eastbourne (Fig. 2) and Raia del Pedale (35), indicating a return to more expanded oceanic anoxia. Interestingly, the recovery of $\delta^{238}U_{carb}$ from this decrease is poorly defined and appears more gradual, unlike the rapid changes in $\delta^{238}U_{carb}$ observed for the PCE. The lack of a distinct post-OAE 2 recovery may indicate a lingering degree of anoxia after the CIE, or that insufficient time is recorded in these sections to observe the complete restabilization of the U and C cycles.

Both AE1 and AE2 are coupled to increased global temperatures, as indicated by $\delta^{18}O$ in Eastbourne (Fig. 2) and organic geochemical proxies in North Atlantic sites (34, 42, 43, 45). Moreover, there is a coupled relationship between decreasing $\delta^{238}U_{carb}$ and $\delta^{7}Li$ during both AE1 and AE2 (Fig. 2), which is suggestive of a shift to a more congruent weathering regime [greater primary mineral dissolution than secondary mineral formation (8, 48)] during these two anoxic intervals. These two intervals are also accompanied by independent evidence for an enhanced hydrological cycle (42), together suggesting two discrete periods of enhanced global weathering flux. In contrast to AE1 and AE2, the increasing $\delta^{238}U_{carb}$ and reoxygenation during the PCE corresponds to cooler temperatures and drier conditions (34, 42, 45), as well as the recovery of $\delta^{7}Li$ to more positive values. The coupling of datasets therefore empirically supports the hypothesized link between enhanced weathering activity under warmer climates, increased nutrient fluxes, heightened productivity, and expanded oceanic anoxia (1, 8, 9, 42). Furthermore, the first interval of decreasing $\delta^{7}Li$ and $\delta^{238}U_{carb}$ (AE1) also temporally corresponds with a prominent decrease in osmium (Os) isotopes to more unradiogenic, basalt-like signatures that marks the main phase of LIP emplacement associated with the CIE (5–8). The return to more radiogenic Os isotope signatures is not seen until after the PCE (5–7), reflecting a degree of continued volcanism across the cooling event, although two separate peaks in sedimentary Os concentrations may indicate multiple phases of heightened volcanic activity (5). LIP activity is therefore likely to have driven the two intervals of enhanced weathering activity and resulted in expanded oceanic anoxia.

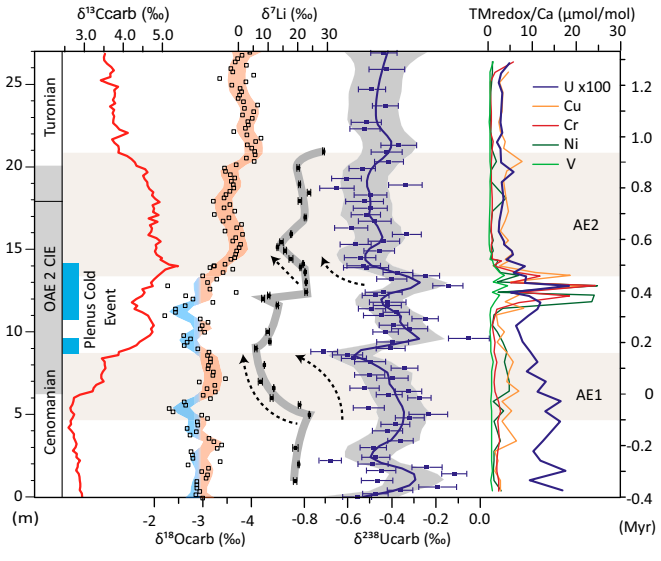

Fig. 2. Complementary geochemical datasets ($\delta^{13}C$, $\delta^{18}O$, and $\delta^{7}Li$) (8, 34), together with the $\delta^{238}U_{carb}$ and TM_{redox} datasets for Eastbourne (35). AE1 and AE2 are identified from coupled negative $\delta^{238}U_{carb}$ excursions and TM_{redox} decreases. Unusual boreal faunas (blue bar) and less negative $\delta^{18}O$ are indicative of cooler waters and mark the PCE (35, 38, 56). Black dashed arrows indicate periods of broad coupling between $\delta^{7}Li$ and $\delta^{238}U_{carb}$. The positive $\delta^{13}C$ excursion (34) is traditionally used to define OAE 2 (gray shading). Timescale (right axis) is based on estimates for OAE 2 of up to ~900 ky (4) and a linear age model, with 0 ky marking the start of the CIE.

A Biogeochemical Model for OAE 2. We use a C–P–U model (*Supporting Information*) to examine whether plausible fluxes of CO_2 from LIP activity can indeed drive the magnitude of changes observed in $\delta^{238}U_{carb}$, U/Ca, and $\delta^{13}C$ at Eastbourne. The model is informed by previously established biogeochemical models (11, 13, 49–52) and calculates the coupled dynamics of C, P, and U cycling associated with changes in temperature, weathering, and oceanic anoxia, in response to hypothesized CO_2 perturbations. The C, P, and U cycles are coupled together with the following processes (Fig. S2): (*i*) LIP CO_2 emission, which acts as a source of C; (*ii*) seafloor spreading, which acts a source of C and a sink of U; (*iii*) silicate weathering, which is a sink of C and a source of P and U; (*iv*) primary production of organic matter, which is controlled by P availability and whose burial is a sink of C; and (*v*) oxygen demand in the ocean, which is controlled by primary productivity and organic matter remineralization rates, and determines the extent of seafloor anoxia and the burial of U(IV) in anoxic sinks. The burial of organic C also results in an input of O_2 to the atmosphere. The U isotope mass balance is included in the model, allowing calculated $\delta^{238}U_{sw}$ to trace the predicted extent of seafloor anoxia, while accounting for changes in U inputs linked to

silicate weathering. Similarly, $\delta^{13}C$ traces relative changes in the sources and sinks of inorganic and organic C.

The model is set up for mid-Cretaceous boundary conditions, and the sensitivity to uncertainty in these parameters is discussed in *Supporting Information*. Background atmospheric O_2 is a particularly important boundary condition. Varying O_2 in the model serves as a convenient way to account for uncertainty in the preexisting degree of anoxia during the pre-OAE 2 interval, and hence the size of the ocean U reservoir (Fig. 3) and the sensitivity of the U cycle to CO_2 perturbations. Estimates of mid-Cretaceous atmospheric O_2 suggest greater than modern levels (49, 51, 53). Here, three baseline settings [O_2 = 1.0, 1.1, and 1.2 times present atmospheric levels (PAL)] are used to provide an envelope of uncertainty that reasonably captures pre-OAE 2 conditions, satisfies U cycle constraints, and covers the range of uncertainty in $\delta^{238}U_{carb}$ (Fig. 2). The highest O_2 concentration setting (1.2 PAL) is the least sensitive to CO_2 perturbations and predicts modern levels of pre-OAE seafloor anoxia (0.3%) with the largest oceanic U reservoir [120% of today's size (16)], and a higher baseline $\delta^{238}U_{sw}$ of –0.30‰ [compared with modern seawater of –0.39 ± 0.01‰ (18, 21, 25, 30, 54)].

AE1. Two CO_2 emission pulses were modeled, corresponding to AE1 and AE2, where the rate of CO_2 injection was kept constant for two discrete intervals of 150 ky. According to the C–P–U model, the $\delta^{238}U_{carb}$ excursion during AE1 can be explained by a CO_2 degassing event of 0.9 to 2.25 × 10^{18} mol C (i.e., 0.6 to 1.5 × 10^{13} mol C·y^{-1}), which represents ∼7 to 19% of current total degassing estimates for the combined Caribbean and Madagascar LIPs (*Supporting Information*). This perturbation results in an increase of atmospheric CO_2 to 3.4 to 4.8 PAL (Fig. 3) and warming of 1.1 °C to 2.3 °C, similar to independent proxy reconstructions (39, 41, 45). The resultant increase in silicate weathering drives a ∼16 to 39% increase in P input (F_{Pw}; Fig. S4), thereby increasing seawater P concentrations ([P]), promoting the expansion of anoxia and the sequestration of reduced U(IV), and preferentially ^{238}U, in anoxic sediments. The responses of ocean nutrient levels, anoxia, and $\delta^{238}U_{sw}$ are delayed compared with the CO_2 emission, with the maximum extent of seafloor anoxia occurring up to ∼100 ky after the end of the CO_2 injection, and covering between 8% and 15%

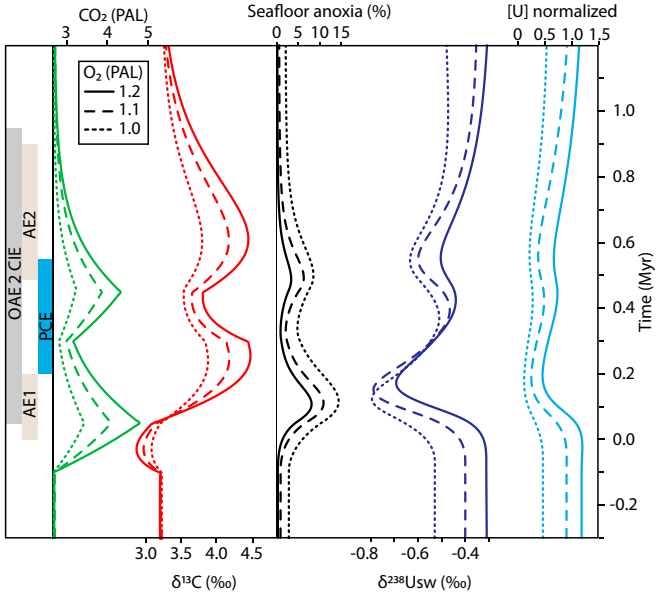

Fig. 3. C–P–U model outputs in relation to events of OAE 2 identified in the $\delta^{238}U_{carb}$ dataset of this study. Time (vertical axis) is given relative to the approximate start of the CIE, as in Fig. 2.

of the total seafloor area (Fig. 3 and Fig. S4). This temporal lag is a function of the positive P feedback mechanism (Fig. S4). When overlain by anoxic waters, sedimentary P burial efficiency is decreased (10, 11, 50, 51) due to (*i*) the decreased flux of P absorbed to Fe oxides (F_{FeP}) and (*ii*) an increased C/P of buried organic matter [$(C/P)_{organic}$], which suppresses productivity-driven increases in the burial of organic bound P (F_{OrgP}). These processes inhibit seawater P depletion in the model and fuel further productivity even when external nutrient inputs are declining, a result which is consistent with published sedimentary P data for OAE 2 (12).

PCE. Carbon sequestration from silicate weathering and the burial of marine-derived organic matter increase during AE1 by 16 to 30% and 20 to 33%, respectively, compared with pre-OAE 2 conditions (Fig. S4). These processes drive the decrease of atmospheric CO_2 after the LIP emission ended, resulting in a temperature and weathering decrease, and hence also a decrease in F_{Pw} (Fig. S4). The combination of decreased F_{Pw}, continued high Ca-bound P burial (F_{CaP}), and high F_{OrgP} burial leads to a [P] decrease (Fig. S4), and hence biological productivity also decreases. The burial of organic matter under anoxic conditions further drives a minor (∼0.02 PAL) net increase in atmospheric O_2 during AE1 (Fig. S4). As a result of these controls, ocean oxygenation progresses and is positively reinforced by the enhanced P removal from increased F_{FeP} burial and decreased $(C/P)_{organic}$ (Fig. S4). In response, $\delta^{238}U_{sw}$ recovers relatively quickly as oceanic anoxia declines, due to the depleted global U reservoir, while [U] recovers more slowly, reaching maximum values up to 100 ky later (Fig. 3). This process could explain the stratigraphic lag between increasing $\delta^{238}U_{carb}$ and U/Ca during the PCE (Figs. 1 and 2; see the discussion below). During the onset of oxygenation and increase in $\delta^{238}U_{sw}$, $\delta^{13}C$ also continues to rise owing to the slower dynamics of the larger C reservoir, again consistent with the trends shown at Eastbourne for the start of the PCE (Fig. 2). Eventually, the decreased burial of organic matter, and thus isotopically light carbon, during the reoxygenation episode begins to generate the carbon isotope "trough" that is used for the chemostratigraphic correlation of the PCE (35, 45, 55, 56).

Despite the $\delta^{238}U_{carb}$ increase during the PCE being consistent with the observations of cooler conditions and local benthic reoxygenation (35, 36, 44–47, 57), the magnitude and abrupt rise of the $\delta^{238}U_{carb}$ at Eastbourne is difficult to simulate with the C–P–U model, assuming that this feature is not an artifact of a condensed sedimentary interval. Indeed, the modeled $\delta^{238}U_{sw}$ recovery better corresponds to the later phase of the PCE, when TM_{redox} also recover. The rapidity of the $\delta^{238}U_{carb}$ increase, and delay of the TM_{redox} enrichments, implies a greater sensitivity of $\delta^{238}U_{carb}$ to changing redox conditions, compared with trace metal concentrations. Such sensitivity was likely driven by an additional decrease in the dynamic residence time of U, already greatly reduced to a minimum of ∼45 ky (O_2 = 1 scenario) during AE1, due to the burial of U(IV) in anoxic sinks. This reduction might have been accomplished by further U drawdown in the "hypoxic" U sink [i.e., sediments that are reducing at depth, beneath a fully or poorly oxygenated water column (19)], which is not accounted for in the model, and would have had little impact on $\delta^{238}U_{carb}$. Under such conditions, $\delta^{238}U_{carb}$ would more precisely capture the onset of reoxygenation than TM_{redox}. Alternatively, this model–data discrepancy may be explained by the oxidation and loss of U from shales previously deposited under anoxic conditions, as has been observed in modern continental margin sediments (58), and is similar to the mechanism proposed to explain transiently light $\delta^{34}S_{CAS}$ values during the PCE (15, 35). This additional supply of isotopically heavy U to the ocean would act to amplify the $\delta^{238}U_{sw}$ increase due to the decrease in anoxic sinks, and could further explain the faster response compared with TM_{redox}. It is also plausible that reoxygenation could have been accelerated by mechanisms not considered in our model, such as sea level or

temperature changes (9, 59), or the additional supply of O_2 caused by pyrite burial (49, 53).

AE2. An assumed second CO_2 injection, of lesser magnitude (0.4 to 1.05×10^{13} mol C·y^{-1}) but of the same duration as the first event, generates a return to warmer conditions after the PCE. This increase in temperature results in a return of widespread anoxia and a smaller negative shift in $\delta^{238}U_{sw}$ by –0.2‰, equivalent to an expansion of oceanic anoxia of 3 to 8% of the total seafloor area. This modeled CO_2 injection also results in the addition of isotopically light carbon to the ocean–atmosphere system that augments the decrease in ^{12}C-enriched carbon burial during the PCE reoxygenation episode, thereby accelerating the development of the $\delta^{13}C$ trough of the PCE. Despite this minor negative excursion, relatively elevated $\delta^{13}C$ values occur throughout the entire OAE 2 interval, owing to the slower dynamics of the relatively large carbon reservoir.

Wider Implications for OAEs. Characterizing the timing, duration, and extent of oceanic anoxia during OAE 2 is fundamental to understanding the driving mechanisms of these extreme perturbations to the carbon cycle and climate system. In an attempt to replicate the distribution of anoxia indicated by local redox proxies, Earth system modeling suggests 50% of the global ocean volume was dysoxic or anoxic (9), while the shale-derived $\delta^{238}U$ estimate suggests only 1 to 2% of the seafloor was overlain by anoxic waters (14). By contrast, the carbonate-derived $\delta^{238}U$ dataset presented here provides a better systematic resolution of the timing and magnitude of ocean deoxygenation (Fig. 1), suggesting that between 8% and 15% of the seafloor was overlain by an anoxic water column. This reconstruction is in close agreement with recent estimates from thallium isotopes (60) and is compatible with 2 to 5% of seafloor being euxinic, based on modeling of the sulfur isotope and molybdenum isotope systems (15, 46, 61), as this extreme chemical state would only make up a fraction of the total anoxic ocean, and $\delta^{238}U$ does not discriminate between anoxic and euxinic redox states. The importance of differentiating these two redox states is increasingly being recognized for periods of expanded anoxia (e.g., ref. 62). Crucially, the high resolution of the $\delta^{238}U_{carb}$ data uniquely resolves at least two fluctuations between episodes of globally expanded and contracted anoxia during the traditionally defined OAE 2 interval. Such findings are likely applicable for other OAEs where there are suggestions of local redox and temperature variability, such as the Aptian OAE 1a (1).

The C–P–U model successfully generates the magnitude of U isotope excursions through fairly conservative CO_2 degassing levels and subsequent changes in global temperature. These amounts of CO_2 degassing probably represent upper estimates, since the model does not consider many contributory deoxygenation mechanisms, including the inverse relationship between temperature and O_2 solubility, or changes in O_2 supply through variable ocean ventilation rates (9). We suggest that these additional mechanisms are of second-order importance to changes in terrestrial weathering for driving OAE 2, although they could help refine our understanding of the precise temporal and geographical distribution of oceanic redox changes.

In summary, the coupled geochemical and modeling approach adopted here for OAE 2 allows for an internally consistent examination of global-scale deoxygenation during carbon cycle perturbation events. The U isotope dataset highlights globally significant oscillations in oceanic redox conditions within the traditionally defined OAE 2 interval that are closely coupled to changes in global temperature and hydrological regime. The C–P–U model successfully reproduces the trends in $\delta^{238}U_{carb}$ through discrete atmospheric CO_2 injections, suggesting that the exceptional longevity of OAE 2 was the result of multiphase LIP activity.

Materials and Methods

U Isotope Analysis. Carbonate samples were mechanically cleaned for weathered surfaces. Sample powders underwent oxidative–reductive cleaning (63, 64), before selective digestion using 1 M buffered sodium acetate. U isotope composition was determined using a ^{236}U–^{233}U double spike to correct for instrumental mass fractionation, where U was preconcentrated by coprecipitation and purified by ion exchange chromatographic procedures using a single column packed with UTEVA resin (Eichrom Technologies) (20, 21, 23, 65, 66). U isotope measurements were performed by multiple collector inductively coupled plasma mass spectrometer (MC-ICP-MS) at the Centre for Trace Element Analysis, University of Otago (19, 21–23).

Li-Isotope Methods. An additional eight samples were analyzed from the Eastbourne section for Li isotopes, to increase the resolution of the already existing dataset, following the same original protocols (8). Carbonate samples were leached using 0.1 M HCl for 1 h and sample solutions were purified using a two-stage cation-exchange procedure. Analyses were performed by MC-ICP-MS at Oxford University (8).

Coupled C–P–U Model. The box model is a simplified version of elements of the Geochemical Carbon Cycle model (GEOCARB) and the Carbon, Oxygen, Phosphorus, Sulfur, and Evolution (COPSE) Earth system model (11, 13, 49–52), focusing exclusively on the shorter-term processes of the carbon and phosphorus cycles. The model incorporates U reservoirs and the isotopic mass balance equations for C and U isotopes as tracers of the predicted outcomes to assumed CO_2 emission perturbations.

ACKNOWLEDGMENTS. We thank the anonymous reviewers of this work for their constructive input. For their contributions to this work, M.O.C., C.H.S., C.M.M., I.R.C., and H.C.J. were supported by the Royal Society of New Zealand, Marsden Fund Standard Grant UOO1314. T.M.L. was supported by the Natural Environment Research Council "Jurassic Earth System and Timescale" large grant and a Royal Society Wolfson Research Merit Award. P.A.E.P.v.S. was funded by European Research Council Consolidator Grant 682760 - CONTROLPASTCO2.

1. Jenkyns HC (2010) Geochemistry of Oceanic Anoxic Events. *Geochem Geophys Geosyst* 11:Q03004.
2. Watson AJ, Lenton TM, Mills BJW (2017) Ocean deoxygenation, the global phosphorus cycle and the possibility of human-caused large-scale ocean anoxia. *Philos Trans A Math Phys Eng Sci* 375:20160318.
3. Dickson AJ, et al. (2014) The spread of marine anoxia on the northern Tethys margin during the Paleocene-Eocene Thermal Maximum. *Paleoceanography* 29:471–488.
4. Eldrett JS, et al. (2015) An astronomically calibrated stratigraphy of the Cenomanian, Turonian and earliest Coniacian from the Cretaceous Western Interior Seaway, USA: Implications for global chronostratigraphy. *Cretac Res* 56:316–344.
5. Turgeon SC, Creaser RA (2008) Cretaceous Oceanic Anoxic Event 2 triggered by a massive magmatic episode. *Nature* 454:323–326.
6. Du Vivier ADC, et al. (2014) Marine $^{187}Os/^{188}Os$ isotope stratigraphy reveals the interaction of volcanism and ocean circulation during Oceanic Anoxic Event 2. *Earth Planet Sci Lett* 389:23–33.
7. Du Vivier ADC, Selby D, Condon D, Takashima R, Nishi H (2015) Pacific $^{187}Os/^{188}Os$ isotope chemistry and U–Pb geochronology: Synchroneity of global Os isotope change across OAE 2. *Earth Planet Sci Lett* 428:204–216.
8. Pogge von Strandmann PAE, Jenkyns HC, Woodfine RG (2013) Lithium isotope evidence for enhanced weathering during Oceanic Anoxic Event 2. *Nat Geosci* 6:668–672.
9. Monteiro F, Pancost R, Ridgwell A, Donnadieu Y (2012) Nutrients as the dominant control on the spread of anoxia and euxinia across the Cenomanian–Turonian Oceanic Anoxic Event (OAE 2): Model-data comparison. *Paleoceanography* 27: PA4209.
10. Van Cappellen P, Ingall ED (1994) Benthic phosphorus regeneration, net primary production, and ocean anoxia—A model of the coupled marine biogeochemical cycles of carbon and phosphorus. *Paleoceanography* 9:677–692.
11. Handoh IC, Lenton TM (2003) Periodic mid-Cretaceous Oceanic Anoxic Events linked by oscillations of the phosphorus and oxygen biogeochemical cycles. *Global Biogeochem Cycles* 17:1092.
12. Mort HP, et al. (2007) Phosphorus and the roles of productivity and nutrient recycling during Oceanic Anoxic Event 2. *Geology* 35:483–486.
13. Berner RA, Kothavala Z (2001) GEOCARB III: A revised model of atmospheric CO_2 over Phanerozoic time. *Am J Sci* 301:182–204.
14. Montoya-Pino C, et al. (2010) Global enhancement of ocean anoxia during Oceanic Anoxic Event 2: A quantitative approach using U isotopes. *Geology* 38:315–318.
15. Owens JD, et al. (2013) Sulfur isotopes track the global extent and dynamics of euxinia during Cretaceous Oceanic Anoxic Event 2. *Proc Natl Acad Sci USA* 110:18407–18412.
16. Dunk R, Mills R, Jenkins W (2002) A reevaluation of the oceanic uranium budget for the Holocene. *Chem Geol* 190:45–67.

17. Anderson R (1987) Redox behavior of uranium in an anoxic marine basin. *Uranium* 3: 145–164.
18. Andersen MB, et al. (2016) Closing in on the marine $^{238}U/^{235}U$ budget. *Chem Geol* 420: 11–22.
19. Andersen MB, Stirling CH, Weyer S (2017) Uranium isotope fractionation. *Rev Miner Geochem* 82:799–850.
20. Stirling CH, Andersen MB, Warthmann R, Halliday AN (2015) Isotope fractionation of ^{238}U and ^{235}U during biologically-mediated uranium reduction. *Geochim Cosmochim Acta* 163:200–218.
21. Stirling CH, Andersen MB, Potter E-K, Halliday AN (2007) Low-temperature isotopic fractionation of uranium. *Earth Planet Sci Lett* 264:208–225.
22. Hinojosa JL, Stirling CH, Reid MR, Moy CM, Wilson GS (2016) Trace metal cycling and $^{238}U/^{235}U$ in New Zealand's fjords: Implications for reconstructing global paleoredox conditions in organic-rich sediments. *Geochim Cosmochim Acta* 179:89–109.
23. Rolison JM, Stirling CH, Middag R, Rijkenberg MJA (2017) Uranium stable isotope fractionation in the Black Sea: Modern calibration of the $^{238}U/^{235}U$ paleoredox proxy. *Geochim Cosmochim Acta* 203:69–88.
24. Noordmann J, et al. (2015) Uranium and molybdenum isotope systematics in modern euxinic basins: Case studies from the central Baltic Sea and the Kyllaren fjord (Norway). *Chem Geol* 396:182–195.
25. Weyer S, et al. (2008) Natural fractionation of $^{238}U/^{235}U$. *Geochim Cosmochim Acta* 72:345–359.
26. Brennecka GA, Herrmann AD, Algeo TJ, Anbar AD (2011) Rapid expansion of oceanic anoxia immediately before the end-Permian mass extinction. *Proc Natl Acad Sci USA* 108:17631–17634.
27. Dahl TW, et al. (2014) Uranium isotopes distinguish two geochemically distinct stages during the later Cambrian SPICE event. *Earth Planet Sci Lett* 401:313–326.
28. Lau KV, et al. (2016) Marine anoxia and delayed Earth system recovery after the end-Permian extinction. *Proc Natl Acad Sci USA* 113:2360–2365.
29. Elrick M, et al. (2017) Global-ocean redox variation during the middle-late Permian through Early Triassic based on uranium isotope and Th/U trends of marine carbonates. *Geology* 45:163–166.
30. Andersen MB, et al. (2014) A modern framework for the interpretation of $^{238}U/^{235}U$ in studies of ancient ocean redox. *Earth Planet Sci Lett* 400:184–194.
31. Romaniello SJ, Herrmann AD, Anbar AD (2013) Uranium concentrations and $^{238}U/^{235}U$ isotope ratios in modern carbonates from the Bahamas: Assessing a novel paleoredox proxy. *Chem Geol* 362:305–316.
32. Chen X, Romaniello SJ, Herrmann AD, Wasylenki LE, Anbar AD (2016) Uranium isotope fractionation during coprecipitation with aragonite and calcite. *Geochim Cosmochim Acta* 188:189–207.
33. Owens JD, et al. (2012) Iron isotope and trace metal records of iron cycling in the proto-North Atlantic during the Cenomanian-Turonian Oceanic Anoxic Event (OAE 2). *Paleoceanography* 27:PA3223.
34. Tsikos H, et al. (2004) Carbon-isotope stratigraphy recorded by the Cenomanian–Turonian Oceanic Anoxic Event: Correlation and implications based on three key localities. *J Geol Soc London* 161:711–719.
35. Jenkyns HC, Dickson AJ, Ruhl M, Van den Boorn SHJM (2017) Basalt–seawater interaction, the Plenus Cold Event, enhanced weathering, and geochemical change: Deconstructing OAE 2 (Cenomanian–Turonian, Late Cretaceous). *Sedimentology* 64: 16–43.
36. Eldrett JS, Minisini D, Bergman SC (2014) Decoupling of the carbon cycle during Ocean Anoxic Event 2. *Geology* 42:567–570.
37. Snow LJ, Duncan RA, Bralower TJ (2005) Trace element abundances in the Rock Canyon Anticline, Pueblo, Colorado, marine sedimentary section and their relationship to Caribbean plateau construction and ocean anoxic event 2. *Paleoceanography* 20: PA3005.
38. Gale AS, Christensen WK (1996) Occurrence of the belemnite *Actinocamax plenus* in the Cenomanian of SE France and its significance. *Bull Geol Soc Den* 43:68–77.
39. Voigt S, Gale AS, Flögel S (2004) Midlatitude shelf seas in the Cenomanian-Turonian greenhouse world: Temperature evolution and North Atlantic circulation. *Paleoceanography* 19:PA4020.
40. Voigt S, Gale AS, Voigt T (2006) Sea-level change, carbon cycling and palaeoclimate during the Late Cenomanian of northwest Europe; an integrated palaeoenvironmental analysis. *Cretac Res* 27:836–858.
41. Voigt S, Wilmsen M, Mortimore R, Voigt T (2003) Cenomanian palaeotemperatures derived from the oxygen isotopic composition of brachiopods and belemnites: Evaluation of Cretaceous palaeotemperature proxies. *Int J Earth Sci* 92:285–299.
42. van Helmond NA, et al. (2014) A perturbed hydrological cycle during Oceanic Anoxic Event 2. *Geology* 42:123–126.
43. Sinninghe Damsté JS, van Bentum EC, Reichart G-J, Pross J, Schouten S (2010) A CO_2 decrease-driven cooling and increased latitudinal temperature gradient during the mid-Cretaceous Oceanic Anoxic Event 2. *Earth Planet Sci Lett* 293:97–103.
44. Jarvis I, Lignum JS, Gröcke DR, Jenkyns HC, Pearce MA (2011) Black shale deposition, atmospheric CO_2 drawdown, and cooling during the Cenomanian–Turonian Oceanic Anoxic Event. *Paleoceanography* 26:PA3201.
45. Forster A, Schouten S, Moriya K, Wilson PA, Sinninghe Damsté JS (2007) Tropical warming and intermittent cooling during the Cenomanian/Turonian Oceanic Anoxic Event 2: Sea surface temperature records from the equatorial Atlantic. *Paleoceanography* 22:PA1219.
46. Dickson AJ, Jenkyns HC, Porcelli D, van den Boorn S, Idiz E (2016) Basin-scale controls on the molybdenum-isotope composition of seawater during Oceanic Anoxic Event 2 (Late Cretaceous). *Geochim Cosmochim Acta* 178:291–306.
47. Kuhnt W, Luderer F, Nederbragt S, Thurow J, Wagner T (2005) Orbital-scale record of the late Cenomanian–Turonian Oceanic Anoxic Event (OAE 2) in the Tarfaya Basin (Morocco). *Int J Earth Sci* 94:147–159.
48. Pogge von Strandmann PAE, Henderson GM (2015) The Li isotope response to mountain uplift. *Geology* 43:67–70.
49. Bergman JM, Lenton TM, Watson AJ (2004) COPSE: A new model of biogeochemical cycling over Phanerozoic time. *Am J Sci* 304:397–437.
50. Lenton TM, Watson AJ (2000) Redfield revisited: 1. Regulation of nitrate, phosphate, and oxygen in the ocean. *Global Biogeochem Cycles* 14:225–248.
51. Lenton TM, Watson AJ (2000) Redfield revisited: 2. What regulates the oxygen content of the atmosphere? *Global Biogeochem Cycles* 14:249–268.
52. Slomp CP, Van Cappellen P (2007) The global marine phosphorus cycle: Sensitivity to oceanic circulation. *Biogeosciences* 4:155–171.
53. Mills BJ, Belcher CM, Lenton TM, Newton RJ (2016) A modeling case for high atmospheric oxygen concentrations during the Mesozoic and Cenozoic. *Geology* 44:1023–1026.
54. Tissot FL, Dauphas N (2015) Uranium isotopic compositions of the crust and ocean: Age corrections, U budget and global extent of modern anoxia. *Geochim Cosmochim Acta* 167:113–143.
55. Erbacher J, Friedrich O, Wilson PA, Birch H, Mutterlose J (2005) Stable organic carbon isotope stratigraphy across Oceanic Anoxic Event 2 of Demerara Rise, western tropical Atlantic. *Geochem Geophys Geosyst* 6:Q06010.
56. Gale A, Jenkyns H, Kennedy W, Corfield R (1993) Chemostratigraphy versus biostratigraphy: Data from around the Cenomanian–Turonian boundary. *J Geol Soc London* 150:29–32.
57. Friedrich O (2010) Benthic foraminifera and their role to decipher paleoenvironment during mid-Cretaceous Oceanic Anoxic Events–The "anoxic benthic foraminifera" paradox. *Rev Micropaleontol* 53:175–192.
58. Morford JL, Martin WR, Carney CM (2009) Uranium diagenesis in sediments underlying bottom waters with high oxygen content. *Geochim Cosmochim Acta* 73:2920–2937.
59. Ozaki K, Tajika E (2013) Biogeochemical effects of atmospheric oxygen concentration, phosphorus weathering, and sea-level stand on oceanic redox chemistry: Implications for greenhouse climates. *Earth Planet Sci Lett* 373:129–139.
60. Ostrander CM, Owens JD, Nielsen SG (2017) Constraining the rate of oceanic deoxygenation leading up to a Cretaceous Oceanic Anoxic Event (OAE-2: ~94 Ma). *Sci Adv* 3:e1701020.
61. Dickson AJ, et al. (2016) Corrigendum to "Basin-scale controls on the molybdenum-isotope composition of seawater during Oceanic Anoxic Event 2 (Late Cretaceous)." *Geochim Cosmochim Acta* 189:404–405.
62. Poulton SW, Canfield DE (2011) Ferruginous conditions: A dominant feature of the ocean through Earth's history. *Elements* 7:107–112.
63. Bian N, Martin PA (2010) Investigating the fidelity of Mg/Ca and other elemental data from reductively cleaned planktonic foraminifera. *Paleoceanography* 25:PA2215.
64. Boyle E, Rosenthal Y (1996) Chemical Hydrography of the South Atlantic During the Last Glacial Maximum: Cd vs. δ13C. *The South Atlantic* (Springer, New York), pp 423–443.
65. Amelin Y, et al. (2010) U–Pb chronology of the solar system's oldest solids with variable 238 U/235 U. *Earth Planet Sci Lett* 300:343–350.
66. Murphy MJ, Stirling CH, Kaltenbach A, Turner SP, Schaefer BF (2014) Fractionation of $^{238}U/^{235}U$ by reduction during low temperature uranium mineralisation processes. *Earth Planet Sci Lett* 388:306–317.
67. Zhou X, et al. (2015) Upper ocean oxygenation dynamics from I/Ca ratios during the Cenomanian–Turonian OAE 2. *Paleoceanography* 30:510–526.
68. Jenkyns HC, Matthews A, Tsikos H, Erel Y (2007) Nitrate reduction, sulfate reduction, and sedimentary iron isotope evolution during the Cenomanian-Turonian Oceanic Anoxic Event. *Paleoceanography* 22:PA3208.
69. Andersen MB, et al. (2015) The terrestrial uranium isotope cycle. *Nature* 517:356–359.
70. Tessier A, Campbell PG, Bisson M (1979) Sequential extraction procedure for the speciation of particulate trace metals. *Anal Chem* 51:844–851.
71. Canfield DE (1998) A new model for Proterozoic ocean chemistry. *Nature* 396: 450–453.
72. Lenton TM, Daines SJ (2017) Biogeochemical transformations in the history of the ocean. *Annu Rev Mar Sci* 9:31–58.
73. Helly JJ, Levin LA (2004) Global distribution of naturally occurring marine hypoxia on continental margins. *Deep Sea Res Part I Oceanogr Res Pap* 51:1159–1168.
74. Jones CE, Jenkyns HC (2001) Seawater strontium isotopes, Oceanic Anoxic Events, and seafloor hydrothermal activity in the Jurassic and Cretaceous. *Am J Sci* 301:112–149.
75. Mills B, Daines SJ, Lenton TM (2014) Changing tectonic controls on the long-term carbon cycle from Mesozoic to present. *Geochem Geophys Geosyst* 15:4866–4884.
76. Holmden C, Amini M, Francois R (2015) Uranium isotope fractionation in Saanich Inlet: A modern analog study of a paleoredox tracer. *Geochim Cosmochim Acta* 153:202–215.
77. Noordmann J, Weyer S, Georg RB, Jöns S, Sharma M (2016) $^{238}U/^{235}U$ isotope ratios of crustal material, rivers and products of hydrothermal alteration: New insights on the oceanic U isotope mass balance. *Isotopes Environ Health Stud* 52:141–163.
78. Eldholm O, Coffin MF (2000) Large igneous provinces and plate tectonics. *The History and Dynamics of Global Plate Motions*, Geophysical Monograph (Am Geophys Union, Washington, DC), Vol 121, pp 309–326.
79. Thordarson T, Self S (1996) Sulfur, chlorine and fluorine degassing and atmospheric loading by the Roza eruption, Columbia River Basalt Group, Washington, USA. *J Volcanol Geotherm Res* 74:49–73.
80. McManus J, et al. (2006) Molybdenum and uranium geochemistry in continental margin sediments: Paleoproxy potential. *Geochim Cosmochim Acta* 70:4643–4662.
81. Hood AvS, et al. (2016) Integrated geochemical-petrographic insights from component-selective δ238U of Cryogenian marine carbonates. *Geology* 44:935–938.
82. Keller G, Han Q, Adatte T, Burns SJ (2001) Palaeoenvironment of the Cenomanian–Turonian transition at Eastbourne, England. *Cretac Res* 22:391–422.
83. Wray DS, Gale AS (2006) The palaeoenvironment and stratigraphy of Late Cretaceous Chalks. *Proc Geol Assoc* 117:145–162.